Title

Evaluation of sulfur-doped aluminum-substituted manganese oxide spinels for lithium ion battery applications

Authors

Doeff, Marca M.
Hollingsworth, Joel
Shim, Joongpyo
et al.

Publication Date

2002-09-10

Peer reviewed

Evaluation of Sulfur-Doped Aluminum-substituted Manganese Oxide Spinels for Lithium Ion Battery Applications

Marca M. Doeff*, Joel Hollingsworth*, Joongpyo Shim†, Young Joo Lee†, Kathryn Striebel†, Jeffrey A. Reimer†, and Elton J. Cairns†

* Materials Sciences Division and

†Environmental Energy Technologies Division

Lawrence Berkeley National Laboratory

University of California

Berkeley, CA 94720, USA.

Acknowledgments

This work was supported by the Assistant Secretary for Energy Efficiency and Renewable Energy, Office of FreedomCAR and Vehicle Technologies of the U.S. Department of Energy under Contract No. DE-AC03-76SF00098. We would like to thank Dr. Hyun Joo Bang of Illinois Institute of Technology for samples of $Li_{1.02}Al_{0.15}Mn_{1.85}O_{3.96}S_{0.04}$ powders and electrodes, and Dr. Jack Vaughey of Argonne National Laboratory for helpful discussion. Some of this work was previously presented as Abstract 825 at the Centennial Meeting of the Electrochemical Society, Philadelphia, PA, May 2002.

Abstract

Spinels with nominal composition $Li_{1.02}Al_{0.25}Mn_{1.75}O_{3.97}S_{0.03}$, $Li_{1.02}Al_{0.25}Mn_{1.75}O_4$ and $Li_{1.02}Al_{0.15}Mn_{1.85}O_{3.96}S_{0.04}$ have been evaluated for their suitability as positive electrode materials in rechargeable lithium ion batteries for electric (EV) and hybrid electric vehicle (HEV) applications. ^{7}Li magic angle spinning (MAS) NMR, XRD, and EDS experiments indicate that sulfur is most likely present as a trace impurity on the surface of the spinel particles rather than substituting for oxygen ions in the bulk, so it is unlikely to account for the previously reported enhanced cyclability of this material. Rather, the unusual particle morphology produced during calcination of some samples in the presence of sulfur compounds appears to impede (but does not completely prevent) conversion to the tetragonal phase that occurs at 3V vs. Li, and ameliorates the capacity fading associated with it. These materials exhibit reduced rate capability and capacity at 4 V, making them unsuitable for high energy density (EV) or high power density applications (HEV).

Introduction

The synthesis and electrochemical behavior of $LiAl_{0.25}Mn_{1.75}O_{3.97}S_{0.03}$, a novel sulfur-doped spinel, have recently been described.[1, 2] In contrast to other manganese oxide spinels, it has been reported to show excellent reversibility even when cycled at 3V vs. Li or at elevated temperatures. Although power management considerations preclude utilization of capacity on both the 3 and 4V plateaus in batteries for vehicular applications, stable electrode materials that can withstand over-discharge and other abuse conditions are necessary to obtain the desired long cycle life of the cell stacks. Because of severe cost constraints[3] associated with devices intended for electric vehicles (EVs) and hybrid electric vehicles (HEVs), less expensive manganese oxide spinels would make particularly attractive replacements for cobalt and cobalt nickel oxides currently used in lithium ion batteries, provided that cycling problems can be overcome. Spinels may be particularly well suited for HEV batteries, because high energy density is not required, but high power density is.

Capacity fading upon cycling of $Li/LiMn_2O_4$ cells has been attributed to irreversible oxidation of electrolyte,[4, 5] dissolution of manganese ions in acidic electrolyte solutions and formation of defect spinel near the end of charge (particularly above 55 ºC),[6, 7] and disconnection of particles associated with the tetragonal phase conversion that occurs at 3V vs. Li.[8] The latter may also occur at 4V during high-rate discharges.[9] Development of new electrolytes,[10] partial substitution of manganese with lithium[11] or other transition metals,[12] and protective coating of particles with lithium carbonate,[13] zinc oxide,[14] or $LiCoO_2$[15] have substantially improved cyclability in recent years. The severe capacity loss associated with reduction of spinels past an average Mn oxidation state of

3.5 and transformation to a tetragonal phase may, however, still be problematic during high rate discharges.

It is interesting to note that capacity fading associated with discharge onto the 3V plateau is greatly ameliorated for ball-milled spinel samples,[16] and for those obtained through sol-gel synthesis.[17] In addition, several research groups have noted that spinels obtained through electrochemical transformation of orthorhombic $LiMnO_2$[18, 19, 20] or O3-$LiMnO_2$ obtained via ion-exchange of $NaMnO_2$[21] cycle much better at 3V vs. Li than conventionally prepared materials do. This improvement, in some cases, has been attributed to the presence of nanometer sized domains[16, 20] that provide ferroelastic accommodation of transformation strains. This strongly suggests that particle morphologies, grain sizes, and microstructures play a critical, if complex, role in determining the electrochemical reversibility of spinels discharged at 3V.

In light of these observations, the unusual particle morphology of $LiAl_{0.25}Mn_{1.75}O_{3.97}S_{0.03}$ shown in references 1 and 2 is striking, and is probably more relevant to the enhanced capacity retention than the S-doping (to which the authors attribute the improved stability). Partial substitution of S for O in the bulk is not expected to occur in a spinel structure, where the oxygen array is nearly cubic close-packed, because of the large discrepancy in ionic radii (1.32 Å for O^{2-}, 1.84 Å for S^{2-}).[22] It is more probable that the detected S is present as a slight impurity or substitutes exclusively at the surface. It would be rather surprising if trace levels of S present on the surface prevented particle breakdown associated with the stresses of phase conversion at 3V (although other effects, such as slowing Mn dissolution, are plausible).

A goal of this study was, therefore, to better understand the cycling behavior of $LiAl_{0.25}Mn_{1.75}O_{3.97}S_{0.03}$ in view of these facts, and also to determine its potential usefulness as a cathode material for lithium ion batteries intended for hybrid electric vehicle applications.

Experimental

Spinels of approximate compositions $Li_{1.02}Al_{0.25}Mn_{1.75}O_{3.97}S_{0.03}$ and $Li_{1.02}Al_{0.25}Mn_{1.75}O_4$ were synthesized from $Li(CH_3COO)•2H_2O$, $Mn(CH_3COO)_2•4H_2O$, Li_2S (optionally), and $Al(NO_3)_3•9H_2O$ by a modification of the sol-gel procedure described in references 1 and 2, and also by a solid state method. When $Li_{1.02}Al_{0.25}Mn_{1.75}O_4$ was the objective, Li_2S was omitted and enough extra $Li(CH_3COO)•2H_2O$ was used to ensure that a phase pure sample with Li:M ratio of 1.02 (where M=Mn +Al) was produced. All samples were first heated to 500 ºC for 10 hours to decompose the acetates, then ground and reheated to 800 ºC in air for ten hours. A final calcination at 800 ºC under flowing oxygen for ten hours was then carried out. A commercially available $LiMn_2O_4$ spinel from Merck (Selectpur SP30, lot # C50339; 1.01075.1000 EF 291315, EM Industries) and samples of $Li_{1.02}Al_{0.15}Mn_{1.85}O_{3.96}S_{0.04}$ given to us by Dr. Hyun Joo Bang of Illinois Institute of Technology were also investigated. Table 1 summarizes the samples used, the sources, and the designations used throughout this paper to refer to the materials.

A Siemens D5000 diffractometer was used to obtain x-ray powder diffraction patterns on the samples, with monochromized Cu Kα radiation (λ = 1.54 Å). Particle sizes were determined with a Beckman Coulter particle size analyzer (model LS 230, with Small Volume Module), and a scanning electron microscope (ISI-DS 130C dual

stage) with an attached x-ray energy dispersive spectrometer (EDAX model DS130 144-10, with amplifier model 184) was used to determine the approximate composition and to observe the particle morphologies.

^{7}Li MAS NMR experiments were performed at 38.95 MHz on a Bruker AMX-100 spectrometer with a Doty probe equipped with a 7 mm rotor. To prevent the loss of data in the beginning of the free induction decay (FID) due to the probe recovery time, a Hahn echo sequence (90°–τ–180°–τ–acq.) was used; the τ value was rotor synchronized (τ = 1/spinning speed). A 90° pulse width of 1.5 μs and a recycle delay of 0.5 s were used. All experiments were carried out at room temperature and with spinning speeds of 10 kHz. All the spectra were referenced in frequency relative to 1M LiCl aqueous solution at 0 ppm.

The samples were hand ground and passed through a 75 μm sieve before being made into electrodes. Electrode mixtures containing 80 or 84 wt. % active material, 8 wt. % Kynar PVdF binder ((grade 2801-00, lot # 97C8118, Elf Atochem North America, Inc., Technical Polymers Department), 4 or 6 wt. % SFG-6 synthetic flake graphite (Timcal Ltd., Graphites and Technologies) and 4 or 6 wt. % 50% compressed acetylene black in N-methylpyrrolidone were spread onto aluminum foil current collectors using a doctor blade. To some mixtures, a small amount of Pelseal Bonding Agent 65 (Pelseal Technologies, LLC) was added according to the manufacturer's directions to prevent cracking. Electrodes were dried overnight in air and then in a 120ºC vacuum oven for at least 8 hours, and some were roll-pressed prior to use. For coin cells with lithium anodes, 5/8" diameter electrodes were punched out and weighed individually to determine loading. This was typically 5-15 mg/cm^2 of active material. Laminate electrodes

containing the IT sample (see Table 1) were donated to us by Dr. Bang and contained 12 wt. % C black, PVdF binder, and about 2.5 mg/cm^2 active material. Coin cells were made as described in Reference 3 and pressed using a Hohsen 2032 coin cell press. A MacPile II (Bio-Logic, SA, Claix, France) was used for galvanostatic cycling experiments.

A 12-cm^2 pouch cell was assembled with a $Li_{1.02}Al_{0.25}Mn_{1.75}O_{3.97}S_{0.03}$ cathode and a natural graphite anode. The anode consisted of 90% natural graphite (Superior Graphite Co.) and 10% PVdF (Kureha) on a Cu foil current collector. The cathode consisted of 84% $Li_{1.02}Al_{0.25}Mn_{1.75}O_{3.97}S_{0.03}$ (JP), 4% SFG-6 (Timcal Ltd), 4% carbon black, and 8% PVdF on an Al foil current collector. The cathode was pressed before assembly into the cell. The ratio of anode to cathode theoretical capacity was 1.4:1. A minimum amount of electrolyte (1M $LiPF_6$ in EC/DEC, LP40 from EM Science) was used in the cell to unmask issues with respect to electrolyte oxidation, and the separator was Celgard 2300 (thickness 25 μm). This pouch cell was cycled between 3.0V to 4.3V by a Maccor battery cycler at room temperature.

Results and Discussion

Materials Characterization

X-ray powder diffraction patterns were typical of phase-pure manganese oxide spinels for samples listed in Table 1, except for SSS, which contained a trace of Mn_2O_3 as an impurity (<5 wt. %). A lattice parameter of 8.19 Å was calculated for materials made in-house, consistent with the partial Al substitution. The patterns appeared essentially identical to one provided to us of the IT sample (no lattice parameter was given).

Scanning electron microscopy was used to investigate spinel samples. Figures 1 and 2 show representative samples of IT and JP powders, respectively. IT consisted of small, idiomorphic particles about 1-2 μm across, whereas JP was composed of irregularly-shaped particles ranging in size from sub-micron to several microns across. Most particles appeared porous rather than faceted like the IT sample, and were lightly fused together during the calcination process into larger agglomerates. A few particles with smooth edges were observed, although these were rare. Small amounts of sulfur were detected with EDAX in the smooth particles (such as the one in the upper center of Figure 2), but not in the porous or irregular ones. Samples made by sol-gel without Li_2S (GFS) and those made by solid state reactions with (SSS) and without (SFS) Li_2S had similar appearances to that of the JP material. As was the case with JP, sulfur did not appear to be distributed evenly throughout the SSS sample, and was present at levels barely detectable by EDAX.

Porous powders result from the decomposition of acetates and release of CO_2 gas during calcination. The presence of sulfur compounds during heating apparently limits the fusion of particles and results in the greatly altered and unusual particle morphology seen in IT. Excess sulfide ion (in the form of Li_2S) was used during the synthesis of JP and SSS, as with IT. Because it is extremely difficult to control the hydrolysis and oxidation reactions of Li_2S during either sol-gel or solid state processing, the particle morphology seen in IT could not be easily reproduced, however.

Figure 3 shows ^7Li MAS NMR results for the samples listed in Table 1. All spectra contain broad resonances at approximately 520 ppm and large spinning-sideband manifolds, characteristic of the NMR spectra of paramagnetic manganese oxides with an

average manganese oxidation state of close to 3.5.[23] A shift in the peak position to higher frequency and an increase in the breadth of the isotropic resonance, in comparison to the undoped spinel lithium manganese oxide (which is not shown here), are consistent with the increase in the Mn oxidation state and increased variety of the local environments, respectively, caused by the Al substitution. However, there is no noticeable effect on the patterns due to the S-doping. For example, the spectra of GFS, JP, and IT are very similar in peak position and the breadth of the isotropic resonance and the intensity of the spinning sidebands. This lack of spectral change suggests that anionic substitution is not taking place inside the lattice. Peaks for samples made by the sol-gel method (IT, JP, and GFS) are broader than for those made by solid state reaction (SSS and SFS), indicating more variety in the Li local environments of the former. This broadening could arise, for example, if aluminum is not evenly distributed throughout the grains or even the individual unit cells of the spinels.

Lithium coin cells

Figure 4 shows voltage profiles of Li/1M $LiPF_6$, EC-DMC/JP and IT coin cells, discharged at 0.1 mA/cm^2. Electrodes JP3-1a and JP3-2a, which contained 80 wt. % active material and 12 wt. % total carbon (6 wt. % graphite and 6 wt. % carbon black) could be discharged farther than electrodes JP2-1a and JP2-2c, which contained 84 wt. % active material and 8 wt. % total carbon (4 wt. % graphite and 4 wt. % carbon black). IT1, which contained 12 wt. % carbon, performed similarly to JP3-1a and JP3-2a, although the average voltage was somewhat higher. All, however, fell considerably short of the theoretical capacity for $Li_{1.02}Al_{0.25}Mn_{1.75}O_{3.97}S_{0.03}$ (135 mAh/g at ~ 4V vs. Li, assuming that Al is not redox active) contained in the JP electrodes or

$Li_{1.02}Al_{0.15}Mn_{1.85}O_{3.96}S_{0.04}$ (140 mAh/g) contained in the IT electrodes. Discharging cells at somewhat lower current densities did not significantly improve utilization (Figure 5). All the electrodes appeared to be somewhat rate-limited, with capacity falling off as the current density was increased above 0.2 mA/cm^2. The cycling behavior at 4V was typical of spinel materials, with very slight fading apparent (Figure 6), although pressed electrodes (e.g., JP3-2b) performed somewhat better than unpressed ones (e.g., JP3-1a). All cells exhibited some coulombic inefficiencies initially, although improvement to 98-100% was seen after the first few cycles.

JP electrodes could be discharged into the two-phase region at 3V vs. Li (Figure 7), although considerable overpotential was observed (i.e., slope in the profile), limiting the capacity that could be obtained. In contrast, IT electrodes polarized almost immediately when discharged below 3.2V. Decreasing the current density to 50 $\mu A/cm^2$ allowed access to capacity around 3V, although this was even more severely limited than for the JP examples. JP electrodes showed severe capacity fading when cycled over both the 3 and 4V plateaus, as is usually seen with spinel electrodes (Figure 8). IT electrodes, on the other hand, lost capacity more slowly, probably because less material underwent tetragonal phase conversion and the accompanying volume change/strain per cycle.

Figure 9 shows discharges of lithium cells with SSS, GFS, SFS, JP, and SP electrodes containing 8% total carbon (not pressed). All of the Al-substituted materials (SSS, GFS, SFS, and JP) perform worse than the unsubstituted SP sample, which could be nearly fully utilized at current densities of 0.5 mA/cm^2 or higher. Cells containing materials made by solid-state reactions (SSS and SFS) had higher average operating voltages (i.e., less overpotential) than those made by sol-gel (JP and GFS), but capacities

were still lower than expected. As with JP and IT electrodes, a slow fade and some coulombic inefficiency was observed for all the cells cycled on the 4V plateau shown in Figure 10. The behavior of SSS, SFS, and GFS, when cycled over both 3 and 4 V plateaus, resembles that of JP rather than that of IT; i.e., capacity loss is very rapid. The fading rate correlates to the depth of discharge onto the 3V plateau; e.g., it is especially severe for the cell containing electrode SSS-14, which showed less overpotential at 3V than cells containing different samples.

The relatively poor rate capabilities and low capacities at 4V of the JP, IT, SSS, SFS, and GFS samples appear to be intrinsic to the materials, although increasing carbon content in electrodes may ameliorate these to some extent, as Figure 4 suggests. All are highly substituted with Al, whether or not they were processed in the presence of S. Preliminary neutron diffraction studies on substituted manganese oxide spinels suggest that some Al is present in 8a (tetrahedral) sites.[24] Even if the level of ion mixing is low, this could slow diffusion or block access to Li ions in tetrahedral sites, causing a lower than expected capacity upon discharge.

Partial Al substitution in some manganese oxides has been shown to improve capacity retention upon cycling,[25] but this was not observed here (compare SP3 to the other cells in Figure 10, for example). Thus, there appears to be no advantage to using manganese oxide spinels with high Al contents. Low levels of Al doping may protect against overcharge (and possibly Mn dissolution) and thus improve cycling, however, with less negative consequences for energy and power density.

The presence of S in some samples had a slight beneficial effect on 4V discharge capacity for unknown reasons (compare JP to GFS and SSS to SFS in Figure 9), but

preparation method (solid state vs. sol gel) was more influential. This is probably due to the better homogeneity of materials prepared by solid state routes. S content did not appear to influence cycling behavior on the 4V plateau alone, or over both plateaus, with the notable exception of IT. This strongly suggests that the unusual particle morphology exhibited by the IT material, rather than the presence of trace amounts of S, is responsible for slowing the tetragonal phase transition that normally occurs at 3V vs. Li, since other S-containing samples (SSS and JP) did not exhibit the same characteristics. While operating cells over both the 3 and 4V plateaus is not practical from a power management standpoint, reducing the rate of tetragonal phase formation under non-equilibrium conditions should improve cyclability on the 4V plateau, particularly for applications that require high-rate discharges. Thus, manipulating the particle morphology of spinels may be advantageous, although a more reproducible method than processing with Li_2S should be chosen.

Natural graphite/spinel pouch cell

Figure 12 shows the two formation cycles (C/25) for the pouch cell containing a natural graphite and a S-doped spinel (JP) cathode with 8% total carbon. The first charge corresponded to 150mAh/g-cathode active material. This was much larger than observed in the cathode half-cell (coin cell), in part because of the extremely low current density (about 23 $\mu A/cm^2$), and in part due to irreversible processes on both electrodes. During the first discharge, 115 mAh/g was reinserted, somewhat higher than that obtained in coin cell configurations. The irreversible capacity loss for first cycle was 22%, which is mostly attributable to the decomposition of electrolyte and the formation of SEI (solid electrolyte interface) layer on the surface of graphite.[26] This anode shows only 18% first

cycle loss, however, when tested in the same electrolyte vs. Li metal,[27] implying that processes at the cathode are responsible for some of the loss.

Figure 13 shows the performance of the pouch cell during C/2 constant-current cycling. The capacity is lower than shown in Fig.4 due primarily to the higher current density (0.29 mA/cm^2), while the rate of capacity fade is higher than that observed with this cathode in a half-cell (Figure 6). The cell coulombic efficiency was 97% during cycling, which is quite low for this configuration. This anode in a half-cell cycles with essentially 100% efficiency once the formation of the SEI is complete.[27] This, and the coulombic inefficiencies seen in the cathode-containing coin cells suggest that oxidation of electrolyte is occurring. In the pouch cells, there is no reservoir of electrolyte to make up for losses, so capacity fading is severe due to the depletion of the lithium inventory and cell failure occurs rapidly. In the coin cells, which have excess electrolytic solution present, cycling is not impacted as severely.

Conclusions

The electrochemical behavior of Al-substituted spinels prepared with and without Li_2S was studied. The relatively high levels of Al substitution appear to decrease rate capability and capacity at 4V, and S-doping has little effect. One sample prepared by a sol-gel method in the presence of Li_2S exhibited an unusual particle morphology and appeared to undergo tetragonal phase conversion much more slowly when cycled onto the 3V plateau in a lithium half-cell configuration than conventional spinels or the other samples in this study. This phenomenon was previously attributed to S-doping, but other S-doped materials without the unusual morphology did not have this characteristic. This suggests that tailoring the particle morphology of spinels may reduce capacity loss

associated with non-equilibrium tetragonal phase formation on the 4V plateau. However, it is difficult to control the reactivity of Li_2S, so other synthetic methods for obtaining small, idiomorphic particles should be considered.

Acknowledgments

This work was supported by the Assistant Secretary for Energy Efficiency and Renewable Energy, Office of FreedomCAR and Vehicle Technologies of the U.S. Department of Energy under Contract No. DE-AC03-76SF00098. We would like to thank Dr. Hyun Joo Bang of Illinois Institute of Technology for samples of $Li_{1.02}Al_{0.15}Mn_{1.85}O_{3.96}S_{0.04}$ powders and electrodes, and Dr. Jack Vaughey of Argonne National Laboratory for helpful discussion. Some of this work was previously presented as Abstract 825 at the Centennial Meeting of the Electrochemical Society, Philadelphia, PA, May 2002.

References

1. S. H. Park, K. S. Park, Y.K. Sun and K. S. Nahm, *J. Electrochem. Soc.,* **147**, 2116 (2000).

2. Y.-K. Sun, G.-S. Park, Y.-S. Lee, M. Yoashio, and K. S. Nahm, *J. Electrochem. Soc.,* **148**, A994 (2001).

3. M. M. Doeff, A. Anapolsky, L. Edman, T. J. Richardson, and L.C. De Jonghe, *J. Electrochem. Soc.*, **148**, A230 (2001).

4. J. M. Tarascon, W.R. McKinnon, F. Coowar, T. N. Bowmer, G. Amatucci, and D.

Guyomard, *J. Electrochem. Soc.*, **141**, 1421 (1994).

5. F. T. Quinlan, K. Sano, T. Willey, R. Vidu, K. Tasaki, and P. Stroeve, *Chem. Mater.*, **13**, 4207 (2001).

6. S. J. Wen, T. J. Richardson, L. Ma, K. A. Striebel, P. N. Ross, Jr., and E.J. Cairns, *J. Electrochem. Soc.*, **143**, L136 (1996).

7. T. Eriksson, T. Gustafsson, and J. O. Thomas, *Electrochem. Solid-State Lett.,* **5** A35 (2002).

8. M. M. Thackeray, *Prog. Solid St. Chem.,* **25**, 1 (1997).

9. M. M. Thackeray, S. Yang, A. J. Kahaian, K. D. Kepler, E. Skineer, J. T. Vaughey, and S. A. Hackney, *Electrochem. Solid-State Lett.,* **1**, 7 (1998).

10. X. Sun, H. S. Lee, X. Q. Yang, and J. McBreen, *Electrochem. Solid-State Lett.,* **4**, A184 (2001).

11. X. Q. Yang, X. Sun, S. J. Lee, J. McBreen, S. Mukerjee, M. L. Daroux, and X. K. Xing, *Electrochem. Solid-State Lett.,* **2**, 157 (1999).

12. E. Iwata, K. Takahashi, and T. Mori, U.S. Patent 6 168 888 (2001).

13. E. I. Wang, U.S. Patent 5 783 328 (1998).

14. Y.-K. Sun, Y.-S. Lee, M. Yoshio, and K. Amine, *Electrochem. Solid-State Lett.,* **5**, A99 (2002).

15. J. Cho, G. B. Kim, H. D. Lim, C. Kim and S. Yoo, *Electrochem. Solid-State Lett.,* **2**, 607 (1999).

16. S.-H. Kang, J. B. Goodenough, and L. K. Rabenberg, *Chem. Mater*. **13**, 1758 (2001).

17. S.-H. Kang and J. B. Goodenough, *J. Electrochem. Soc.* **147**, 3621 (2000).

18. R. J. Gummow, D. C. Liles, and M. M. Thackeray, *Mat. Res. Bull.*, **28**, 1249 (1993).

19. I. Koetschau, M. N. Richard, and J. R. Dahn, *J. Electrochem. Soc.*, **142**, 2906 (1995).

20. Y.-M. Chiang, H. Wang, and Y.-I. Jang, *Chem. Mater.,* **13**, 53 (2001).

21. A. R. Armstrong and P. G. Bruce, *Nature*, **381**, 499 (1996).

22. *Handbook of Chemistry and Physics*, R. C. Weast, Editor, 68th ed., CRC Press, Inc., Boca Raton, FL (1987-1988).

23. Y. J. Lee, F. Wang, and C. P. Grey, *J. Am. Chem. Soc*.,**120**, 12601 (1998).

24. Personal communication, Dr. Jack Vaughey, Argonne National Laboratory.

25. Y.-M. Chiang, D. R. Sadoway, Y.-I. Jang, B. Huang, and H. Wang, *Electrochem. Solid-State Lett.*, **2**, 107 (1999).

26. D. Aurbach, B. Markovsky, I. Weissman, E. Levi, Y. Ein-Eli, *Electrochim. Acta*, **45**, 67 (1999).

27. J. Shim, K.A. Striebel, J. Power Sources, submitted.

Table 1

Spinel samples used for this study

Spinel nominal composition	Source	Synthesis	Designation
$Li_{1.02}Al_{0.25}Mn_{1.75}O_{3.97}S_{0.03}$	Made in-house	Sol-gel, with Li_2S	JP
$Li_{1.02}Al_{0.25}Mn_{1.75}O_4$	Made in-house	Sol-gel, no Li_2S	GFS
$Li_{1.02}Al_{0.25}Mn_{1.75}O_{3.97}S_{0.03}$	Made in-house	Solid state, with Li_2S	SSS
$Li_{1.02}Al_{0.25}Mn_{1.75}O_4$	Made in-house	Solid state, no Li_2S	SFS
$Li_{1.02}Al_{0.15}Mn_{1.85}O_{3.96}S_{0.04}$	Illinois Inst. of Technology	Sol-gel, with Li_2S	IT
$Li_{1.03\text{-}1.06}Mn_2O_4$	Merck	Selectpur SP30, lot # C50339	SP

Figure Captions

Figure 1. Scanning electron micrograph of sample IT, $Li_{1.02}Al_{0.15}Mn_{1.85}O_{3.96}S_{0.04}$.

Figure 2. Scanning electron micrograph of sample JP, $Li_{1.02}Al_{0.25}Mn_{1.75}O_{3.97}S_{0.03}$.

Figure 3. ^{7}Li MAS NMR patterns for spinel samples. From top to bottom: $Li_{1.02}Al_{0.25}Mn_{1.75}O_4$ made by sol-gel (GFS sample), $Li_{1.02}Al_{0.25}Mn_{1.75}O_4$ made by solid state (SFS sample), $Li_{1.02}Al_{0.25}Mn_{1.75}O_{3.97}S_{0.03}$ made by sol-gel (JP sample), $Li_{1.02}Al_{0.25}Mn_{1.75}O_{3.97}S_{0.03}$ made by solid state (SSS sample), and $Li_{1.02}Al_{0.15}Mn_{1.85}O_{3.96}S_{0.04}$ made by sol-gel (IT sample).

Figure 4. Discharges at 0.1 mA/cm^2 of Li/1M $LiPF_6$, EC-DMC/JP and IT cells. Electrodes are as follows: (—) JP3-1a, containing 12 wt. % total carbon, not pressed, (···) JP3-2a, containing 12 wt. % carbon, pressed, (-----) JP2-1a, containing 8 wt. % carbon, not pressed, and (— — —) JP2-2c, containing 8 wt. % carbon, pressed and (-·-·-·) IT1, containing 12 wt. % C.

Figure 5. Discharges of cell Li/1M $LiPF_6$, EC-DMC/JP3-1a at (—) 50 μA/cm^2 and at (----) 0.1 mA/cm^2. Electrode JP3-1a contains 12 wt. % carbon.

Figure 6. Capacity at 4V as a function of cycle number for Li/1M $LiPF_6$, EC-DMC/JP and IT cells. Electrodes are as follows: (+) IT3, containing 12 wt. % C, discharged at 0.1 mA/cm^2, (□) JP3-1a, containing 12 wt. % total carbon, not pressed, discharged at 0.1 mA/cm^2, (•) JP3-2b, containing 12 wt. % total carbon, pressed, discharged at 0.2 mA/cm^2, and (×) JP2-1a, containing 8 wt. % carbon, not pressed, discharged at 0.1 mA/cm^2.

Figure 7. Discharges of cells Li/1M $LiPF_6$, EC-DMC/JP3-2b at 0.2 mA/cm^2 (----) and Li/1M $LiPF_6$, EC-DMC/IT1 (—) at 50 μA/cm^2. JP3-2b and IT1 electrodes contain 12 wt. % carbon.

Figure 8. Capacity as a function of cycle number for cells Li/1M $LiPF_6$, EC-DMC/JP3-2b (•), discharged at 0.2 mA/cm^2 and Li/1M $LiPF_6$, EC-DMC/IT1 (□), discharged at 50 μA/cm^2, over both 3 and 4 V plateaus. For ease of comparison, the first cycle over both plateaus was designated 1 for both cells; JP3-2b was cycled 81 times and IT1 20 times at 4V prior to discharge below 3V. JP3-2b and IT1 electrodes contain 12 wt. % carbon.

Figure 9. Discharges of cell Li/1M $LiPF_6$, EC-DMC/SP2 at 0.5 mA/cm^2 (—) and Li/1M $LiPF_6$, EC-DMC/SSS-12 (----), SFS-B (···), JP2-1a (— -), and GFS-G (— —) cells at 0.1 mA/cm^2. All electrodes contain 8 wt. % carbon.

Figure 10. Capacity at 4V as a function of cycle number for Li/1M $LiPF_6$, EC-DMC/SP, SSS, JP, GFS, and SFS cells. Electrodes contain 8% carbon, and are not pressed. They are as follows: (+) SP3, discharged at 0.5 mA/cm^2, (△) SSS-15, discharged at 0.1 mA/cm^2, (♦) SFS-D, discharged at 0.1 mA/cm^2, (□) SFS-B, discharged at 0.2 mA/cm^2, and (•) GFS-G, discharged at 0.1 mA/cm^2.

Figure 11. Capacity as a function of cycle number for cells Li/1M $LiPF_6$, EC-DMC/SSS, GFS and SFS cells discharged at 0.1 mA/cm^2 over both 3 and 4 V plateaus. Electrodes contain 8% carbon and are not pressed. They are as follows: SSS-14 (○), GFS-H (■), and SFS-A (×). Cell SFS-A was cycled four times on the 4V plateau prior to being discharged to 3V.

Figure 12. First (——) and second (▬▬) charge and discharge of pouch cell, natural graphite/1M $LiPF_6$, EC-DEC/JP cycled at C/25.

Figure 13. Capacity as a function of cycle number for pouch cell, natural graphite/1M $LiPF_6$, EC-DEC/JP cycled at C/2 between 3.0V and 4.3V.

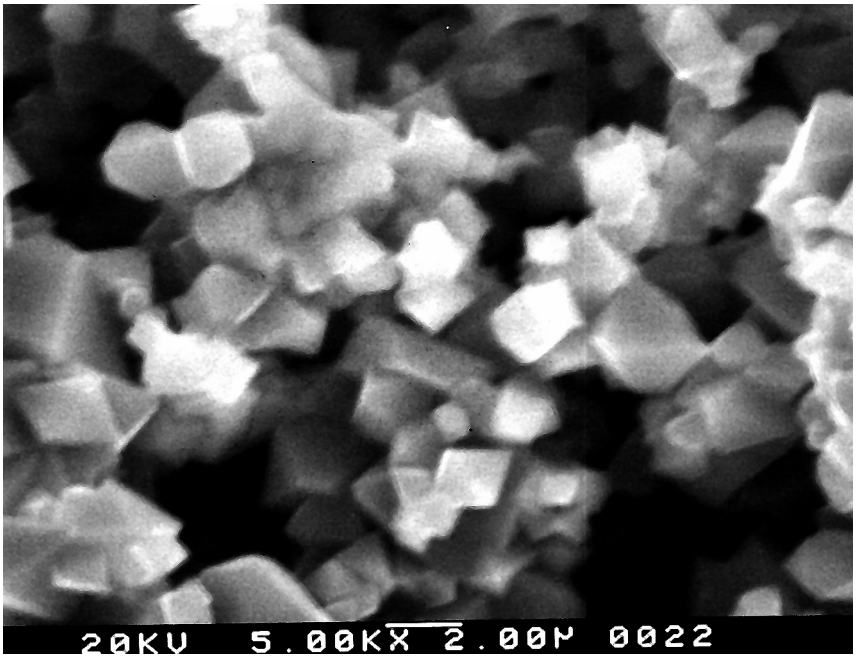

Figure 1.

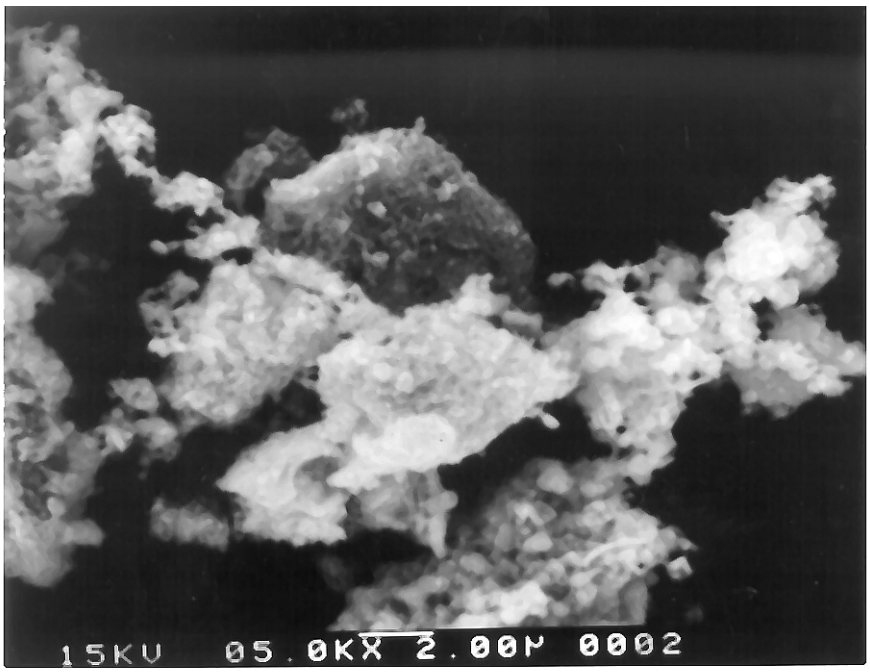

Figure 2.

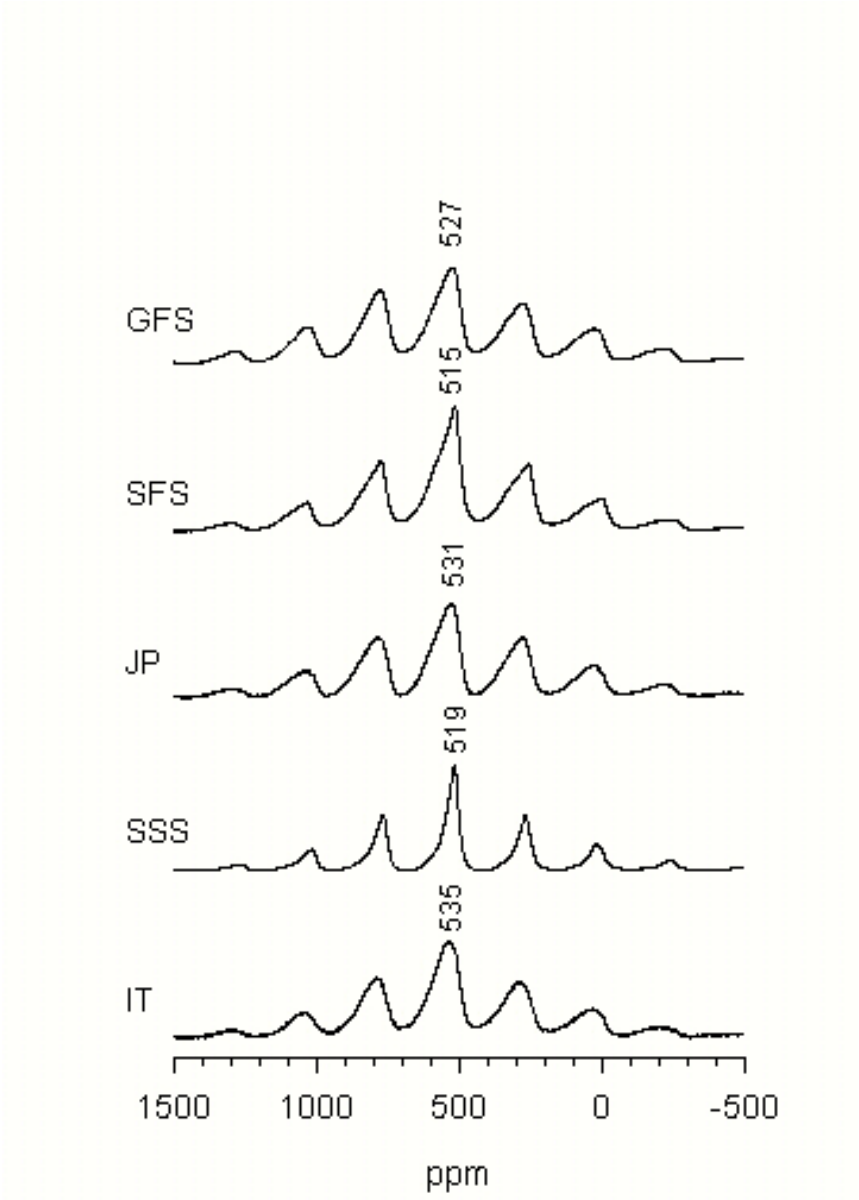

Figure 3.

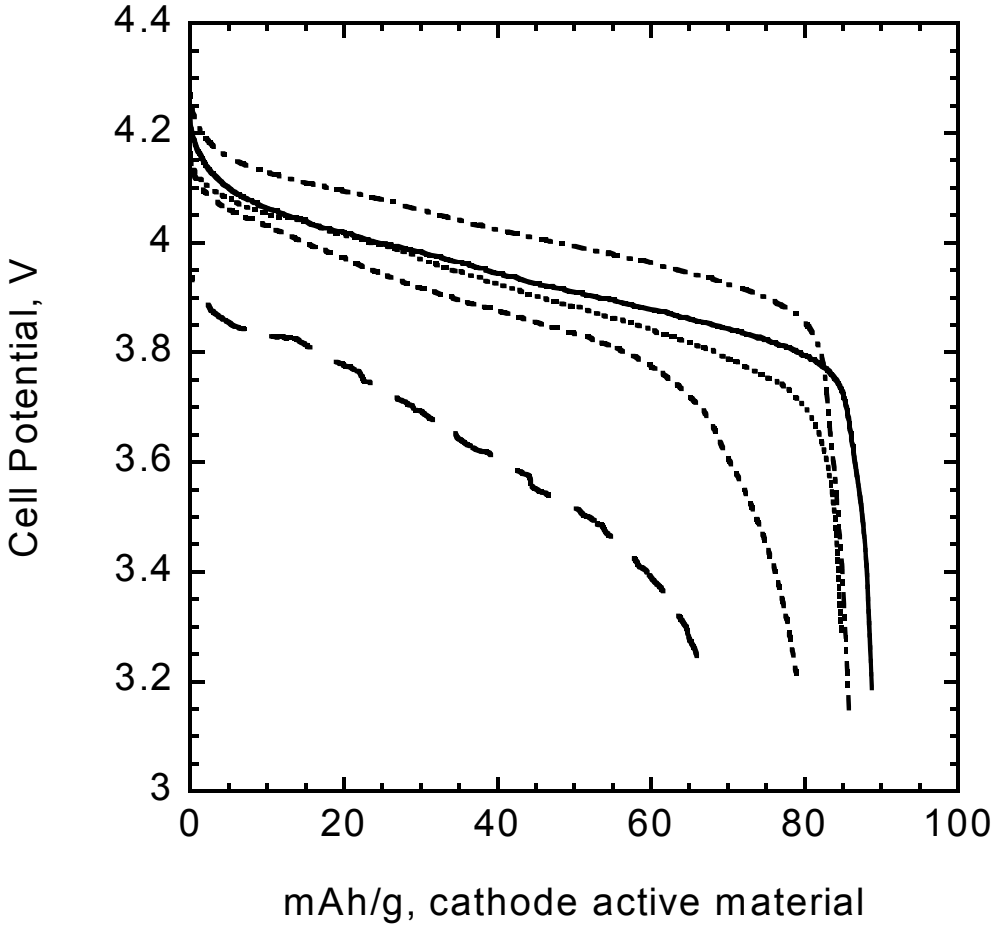
4.4
4.2
4
3.8
3.6
3.4
3.2
3
Cell Potential, V
0
20
40
60
80
100
mAh/g, cathode active material

Figure 4.

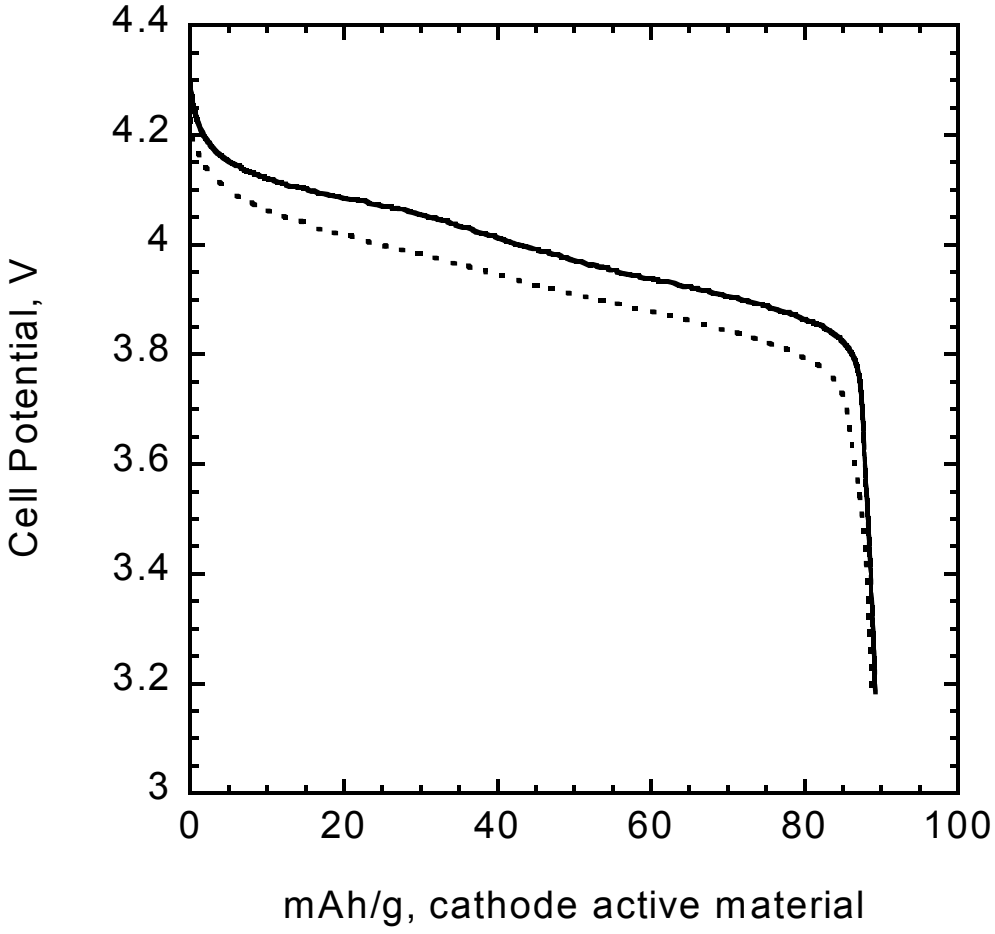
4.4
4.2
4
3.8
3.6
3.4
3.2
3
Cell Potential, V
0
20
40
60
80
100
mAh/g, cathode active material

Figure 5.

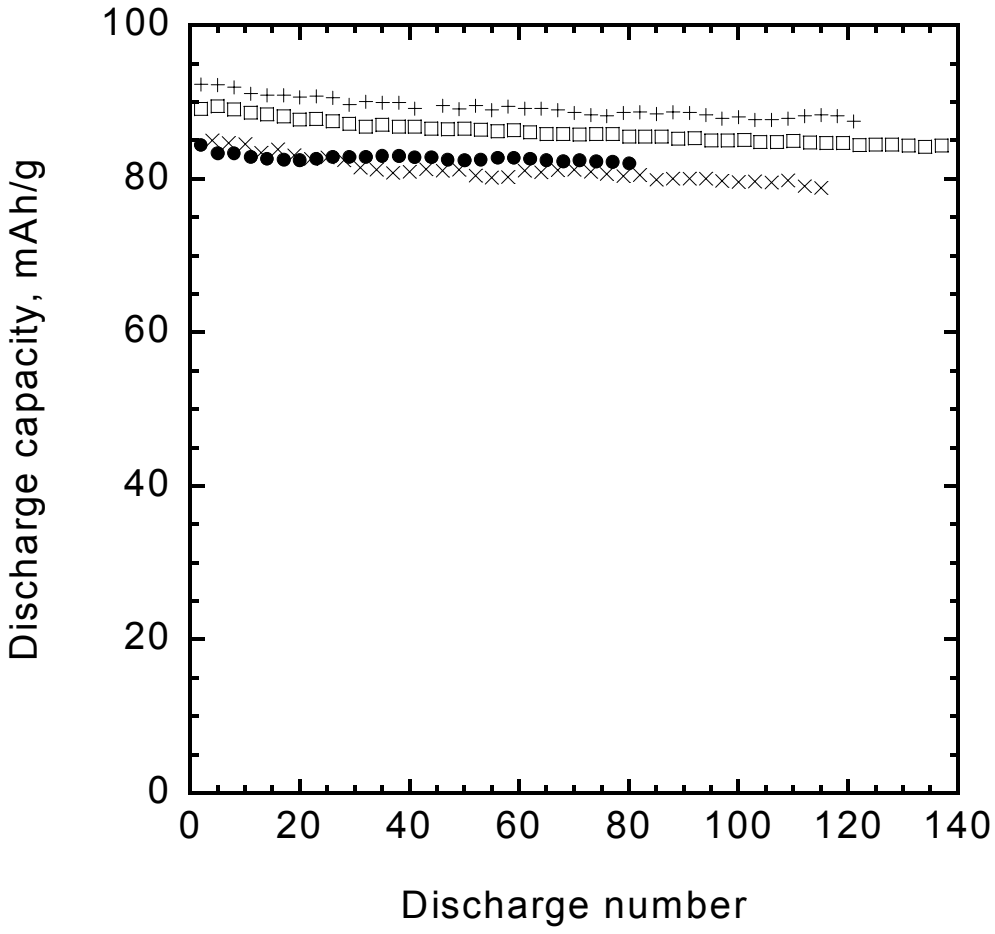
Discharge capacity, mAh/g
Discharge number
0
20
40
60
80
100
120
140

Figure 6

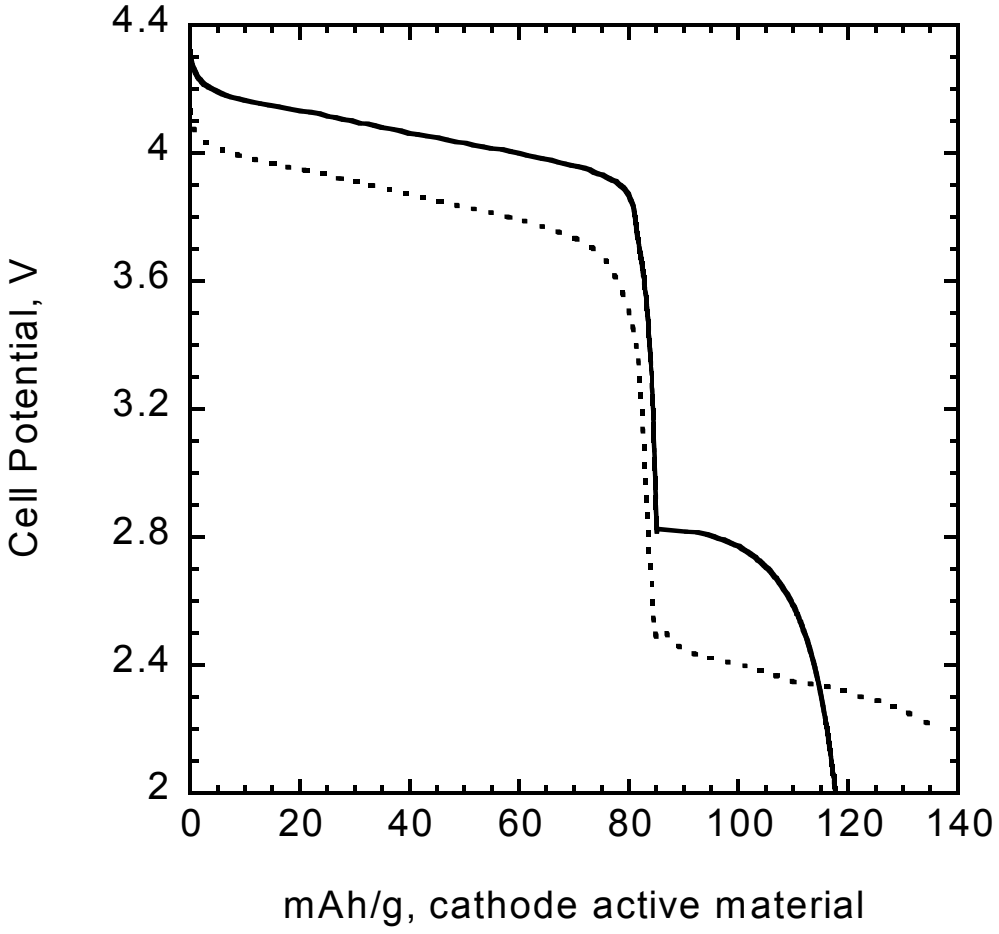
4.4
4
3.6
3.2
2.8
2.4
2
Cell Potential, V
0
20
40
60
80
100
120
140
mAh/g, cathode active material

Figure 7.

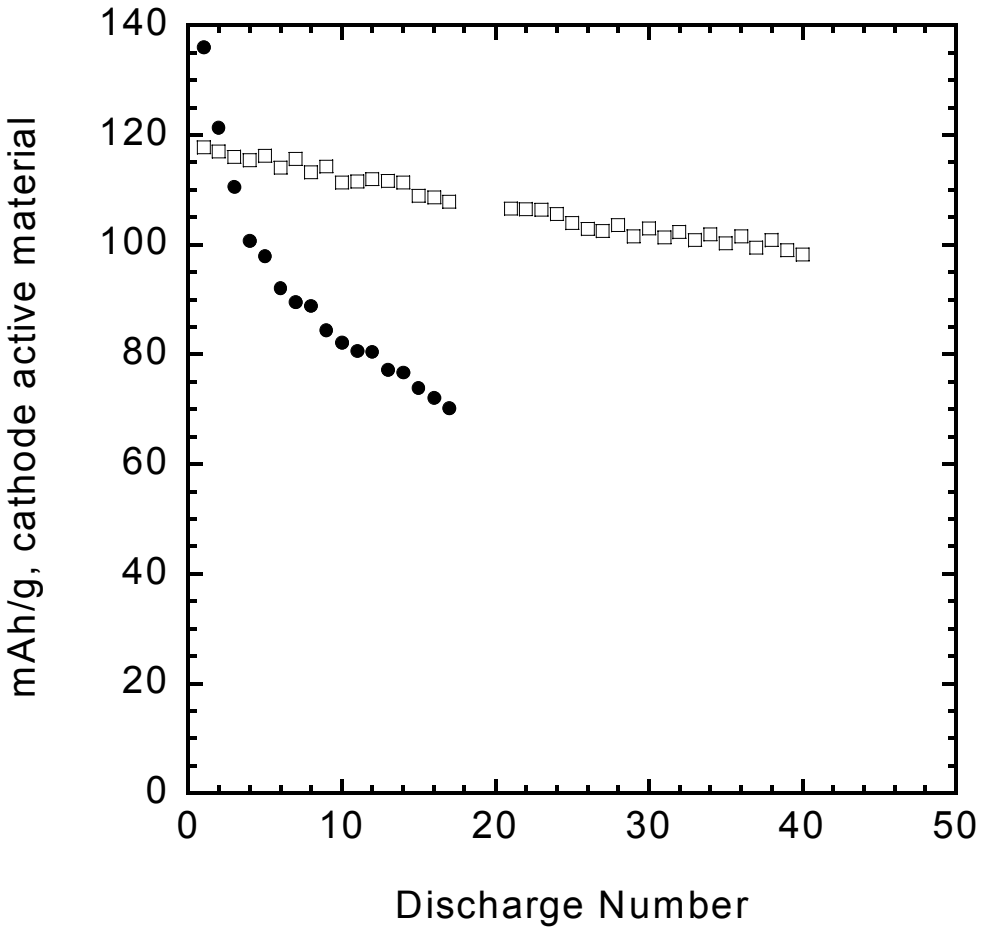
mAh/g, cathode active material
Discharge Number
0
20
40
60
80
100
120
140
0
10
20
30
40
50

Figure 8.

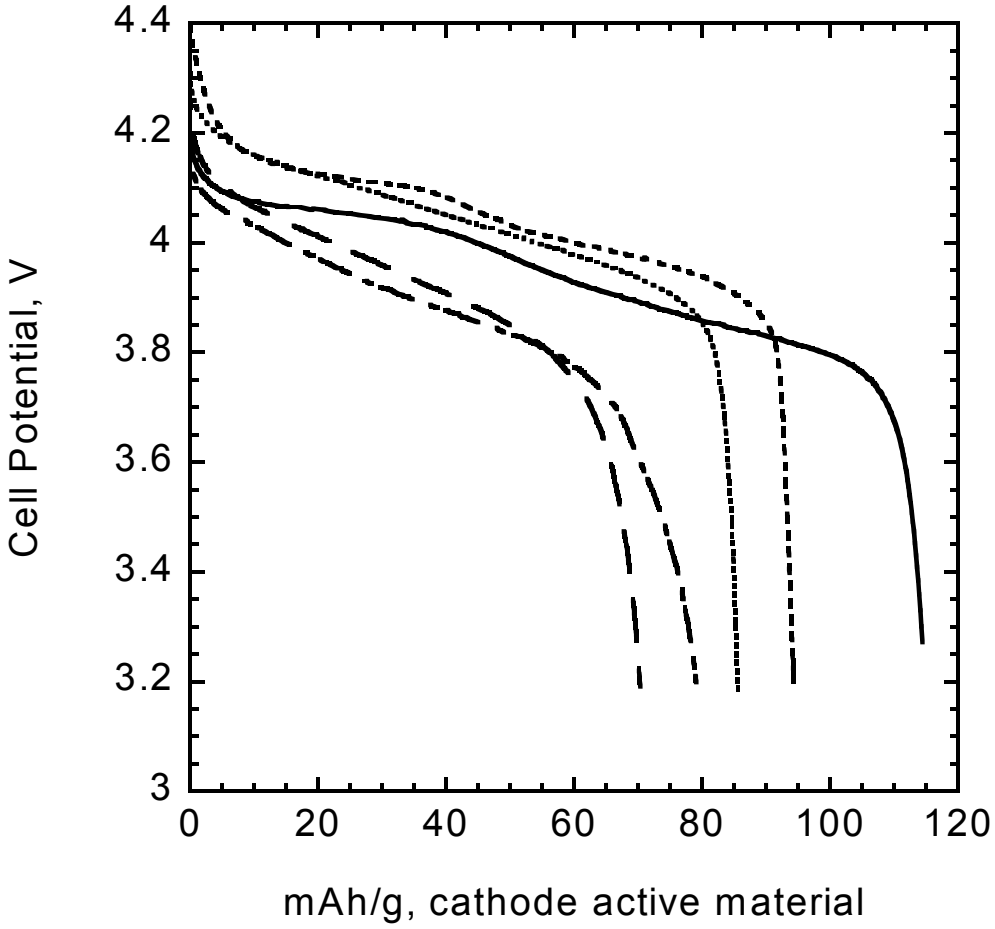
4.4
4.2
4
3.8
3.6
3.4
3.2
3
Cell Potential, V
0
20
40
60
80
100
120
mAh/g, cathode active material

Figure 9.

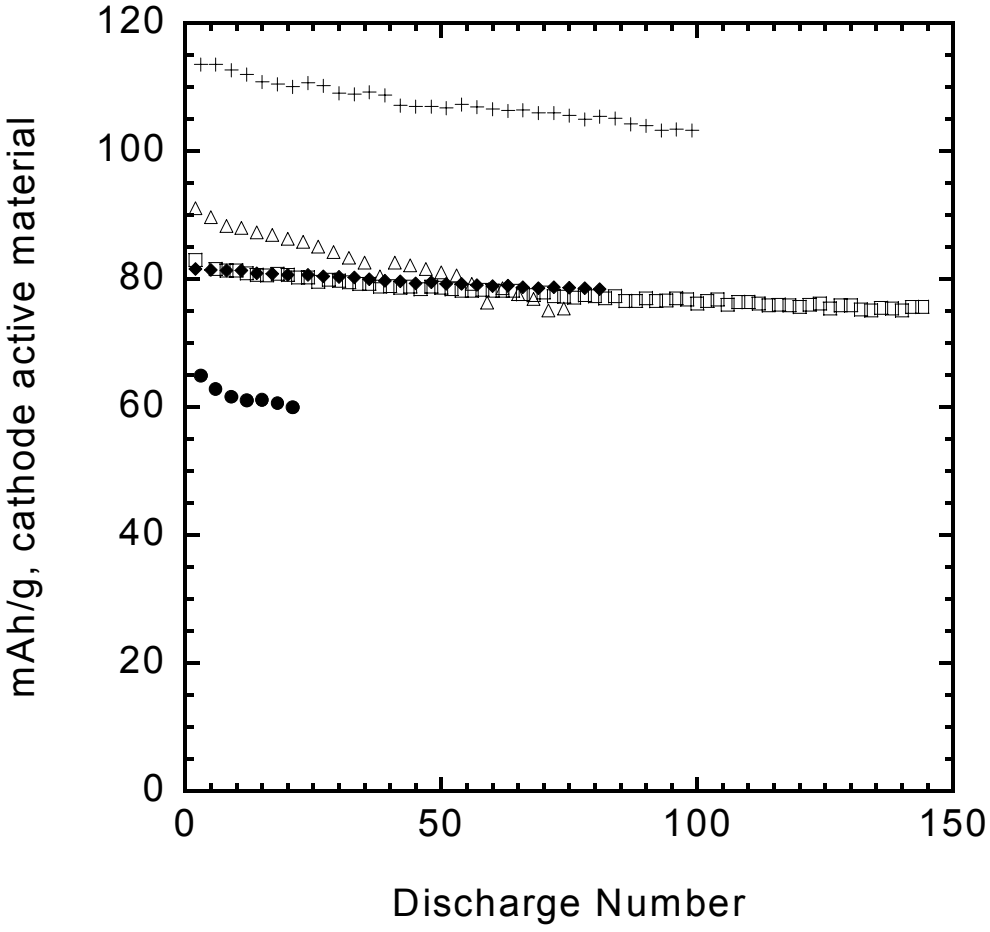
120
100
80
60
40
20
0
0
50
100
150
mAh/g, cathode active material
Discharge Number

Figure 10

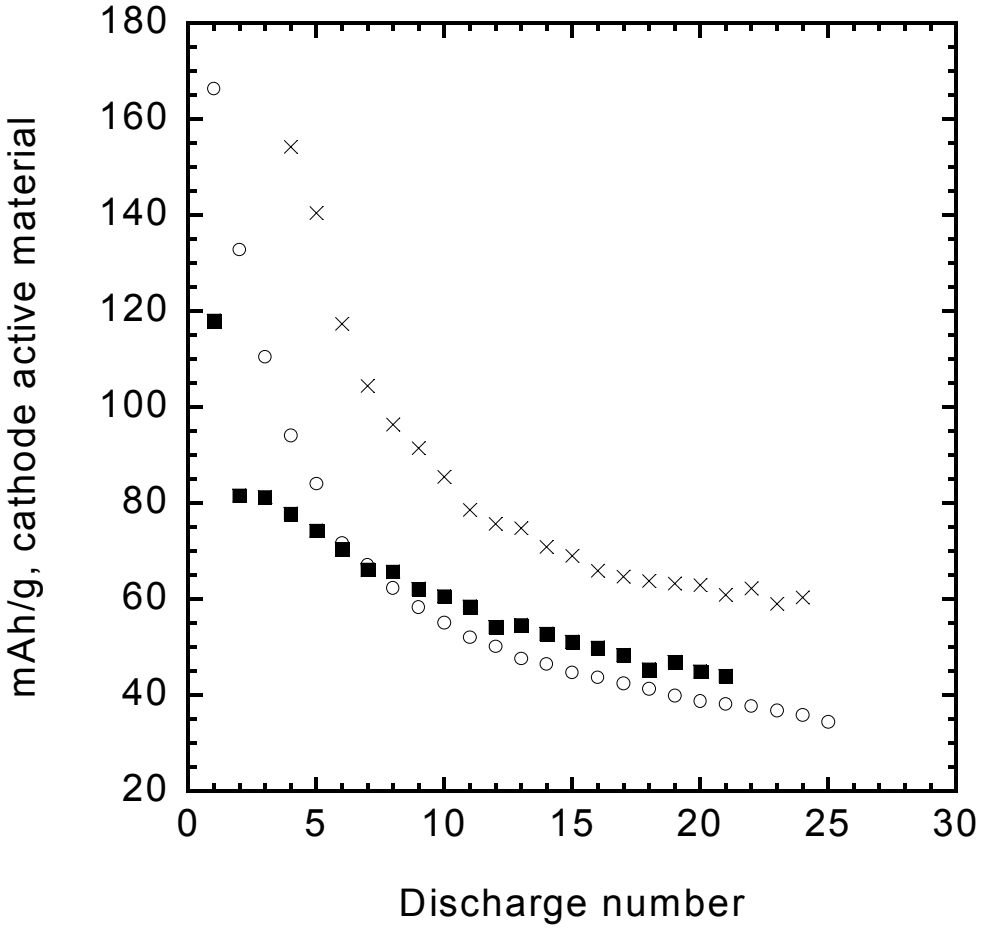
mAh/g, cathode active material
Discharge number
180
160
140
120
100
80
60
40
20
0
5
10
15
20
25
30

Figure 11.

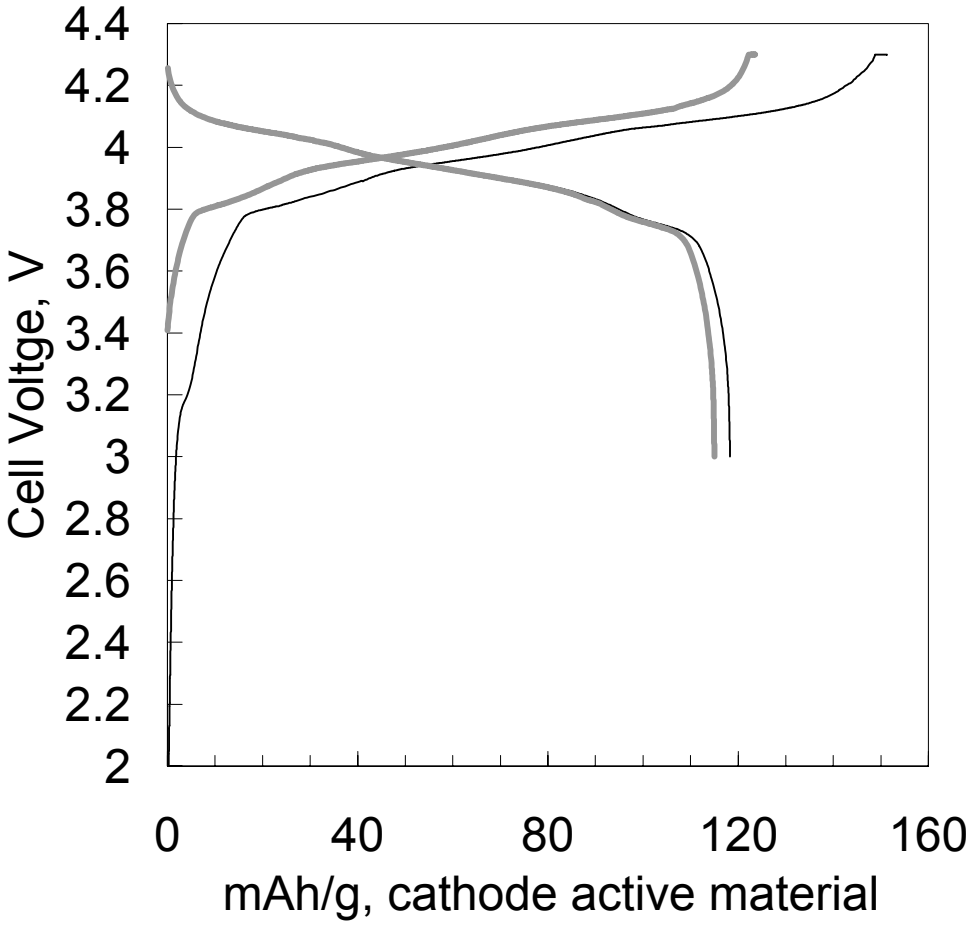
4.4
4.2
4
3.8
3.6
3.4
3.2
3
2.8
2.6
2.4
2.2
2
Cell Voltge, V
0
40
80
120
160
mAh/g, cathode active material

Figure 12.

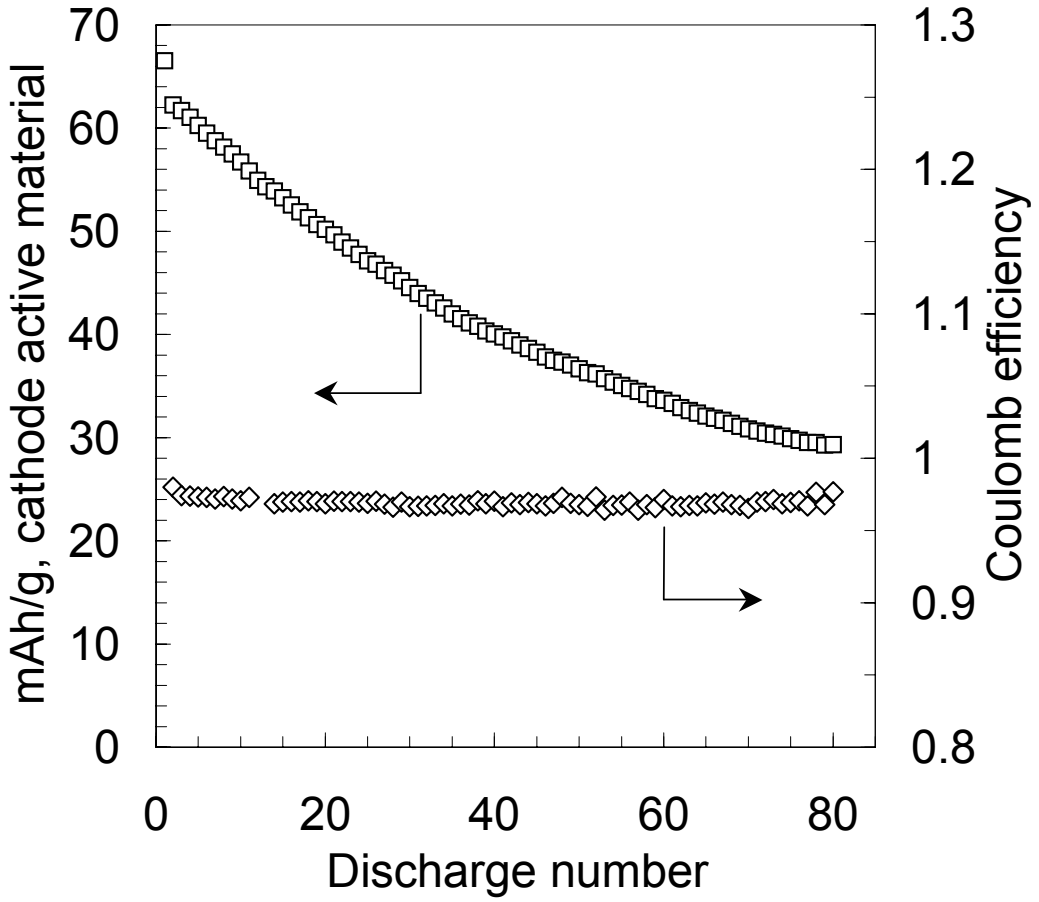
70
60
50
40
30
20
10
0
mAh/g, cathode active material
1.3
1.2
1.1
1
0.9
0.8
Coulomb efficiency
0
20
40
60
80
Discharge number

Figure 13.